

Multiwavelength View of the Inner Spiral of NGC 1365

Iskra V. Strateva^{1*} and S. Komossa^{1*}

¹Max Planck Institut für extraterrestrische Physik, Giessenbachstrasse, 85748 Garching, Germany

Received 2009 February 25

ABSTRACT

We study the extended nuclear emission of the starburst galaxy NGC 1365. A weak obscured AGN and a strong starburst both contribute to the observed X-ray, optical, infrared, and radio emission in the inner 2 kpc. The X-ray emission is spatially resolved, allowing comparison with multiwavelength data that highlights the structures dominating the nuclear region: the AGN, the nuclear spiral, the circumnuclear starburst ring, and nuclear outflow. The ultrasoft X-ray emission $\lesssim 0.5$ keV is spatially coincident with the conical outflow traced by higher excitation optical emission lines like [O III] and [Ne III]. The strong starburst concentrated in super-star clusters in a circumnuclear ring with radius ≈ 1 kpc dominates the 0.5–1.5 keV emission and is visible in radio, molecular CO, and infrared maps of the central kiloparsec. The hard (2–10 keV) emission is dominated by the obscured AGN, but also contributes to the emission from relatively old (~ 7 Myr) but still enshrouded in dust and extremely massive ($10^7 M_{\odot}$) super-star clusters (Galliano et al. 2008), hidden from view in the optical and soft X-ray bands. In the Appendix we present the X-ray spectroscopy and photometry of BL Lac MS 0331.3–3629, a high-energy peaked BL Lac candidate at $z = 0.308$, serendipitously detected in one *Chandra* and five *XMM-Newton* observations of NGC 1365.

Key words: galaxies: individual: NGC 1365 – galaxies: starburst – X-rays: galaxies.

1 INTRODUCTION

Chandra's excellent imaging resolution allows us an unprecedented glimpse of the spatially resolved X-ray emission of nearby galaxies. Unlike the simple nuclear point-source emission characterizing the X-ray view of luminous quasars, nearby starburst galaxies and active galactic nuclei (AGNs) show a plethora of diverse X-ray features: off-center point source emission from X-ray binaries, emission from supernova remnants, diffuse collisionally ionized emission from galactic halos, emission from photoionized narrow line regions (NLRs), as well as the X-ray emission of jets and outflows, including starburst-driven superwinds (e.g., Wang et al. 2001; Fabbiano 2002; Wang 2003; Ogle et al. 2003; Strickland et al. 2004; Read 2006). When combined with optical, radio, and infrared emission maps, the spatially resolved X-ray emission allows us to identify important processes associated with the birth and deaths of stars, the size, place, and composition of regions of recent star formation, as well as to gauge the influence of the AGN on the nuclear regions of galaxies.

The barred supergiant¹ spiral NGC 1365 has been

the target of extensive studies from the radio (e.g., Sandqvist et al. 1995; Stevens et al. 1999, and references therein) to the X-ray band (e.g., Turner et al. 1993; Iyomoto et al. 1997; Komossa & Schulz 1998; Risaliti et al. 2005a,b, 2007). The multiwavelength data on NGC 1365 was recently reviewed in Lindblad (1999). In the X-ray band, there are at least three distinct emission components. The obscured active nucleus (Iyomoto et al. 1997; Komossa & Schulz 1998; Risaliti et al. 2005a,b, 2007), the soft, extended emission (Turner et al. 1993; Komossa & Schulz 1998; Wang et al. 2009), and the X-ray point source populations (Turner et al. 1993; Komossa & Schulz 1998; Soria et al. 2007; Strateva & Komossa 2009).

NGC 1365 is special in the sense that several of its multi-wavelength properties are, at first glance, unusual. (1) The degree of excitation of *narrow* emission-lines detected in optical spectra is actually lower in the core region of NGC 1365 than in the extranuclear regions (e.g., Edmunds et al. 1988; Schulz et al. 1999; Veilleux et al. 2003). (2) While this could be explained by strong core extinction, a *broad* component nevertheless shows up in the Balmer lines (Veron et al. 1980; Edmunds & Pagel 1982; Schulz et al. 1999). The width of the broad-line component is ~ 1600 – 1900 km s⁻¹ and would formally imply a classifica-

* E-mail: strateva@mpe.mpg.de

¹ The $B = 25^m$ arcsec⁻² isophotal radius of NGC 1365 is 30 kpc.

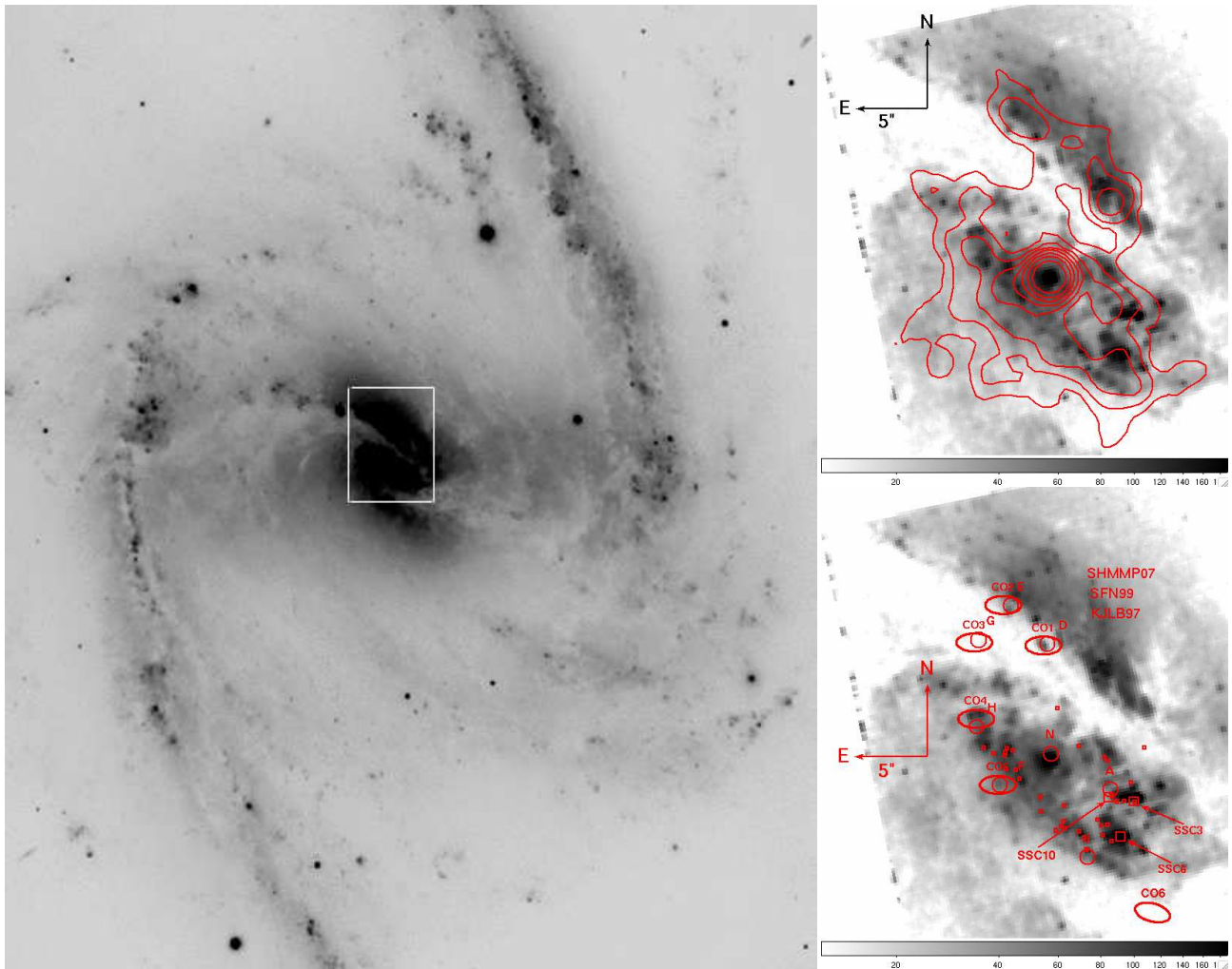


Figure 1. *Left:* Optical VLT image of NGC 1365 with the inner spiral region marked. *Top right:* *HST* WFPC2 F555W image of the inner spiral of NGC 1365 with the 0.3–10 keV band logarithmically-spaced contours from the 2002 *Chandra* observation overlaid in red. *Bottom right:* The circumnuclear starburst ring of NGC 1365 is shown here over the same *HST* image, traced by the optical super-star clusters (the SSCs are denoted by squares; Kristen et al. 1997, KJL97), the radio hotspots (circles; Stevens et al. 1999, SFN99), and the ^{12}CO molecular hotspots (ellipses; Sakamoto et al. 2007, SHMMP07).

tion as narrow-line Seyfert 1 galaxy, even though the other properties of NGC 1365 do not match that classification. (3) Compared to other samples of Seyfert galaxies (Ward et al. 1988), the optical and IR properties of NGC 1365 appear to be off the correlations and trends in multi-wavelength diagrams (Komossa & Schulz 1998). (4) To this adds the recent finding that the X-ray obscuration of NGC 1365, which is unusually variable on very short timescales (e.g., Risaliti et al. 2005a), is likely caused by the broad-line region clouds (Risaliti et al. 2008).

With the key goals in mind of spatially resolving the soft X-ray emission seen with ROSAT and disentangling AGN and starburst components, getting new clues on the multi-wavelength properties of NGC 1365, and studying its population of X-ray sources including the luminous source NGC 1365-X1, we obtained a *Chandra* ACIS-S observation of NGC 1365 on MPE guaranteed time.

In this paper we report on the extended X-ray emission of NGC 1365. We show that the 0.5–10 keV extended nuclear emission originates in the star-forming

ring and nuclear spiral in the inner 2 kpc of NGC 1365, as traced by radio hotspots, molecular CO emission, mid-infrared (MIR) emission, and optically detected super star clusters, while ultrasoft (<0.5 keV) emission traces a nuclear outflow cone (Storchi-Bergmann & Bonatto 1991; Hjelm & Lindblad 1996; Lindblad 1999; Veilleux et al. 2003). Throughout this paper we assume a luminosity distance² of 21 Mpc to NGC 1365. All quoted flux and luminosity uncertainties are 90% confidence limits, unless noted otherwise.

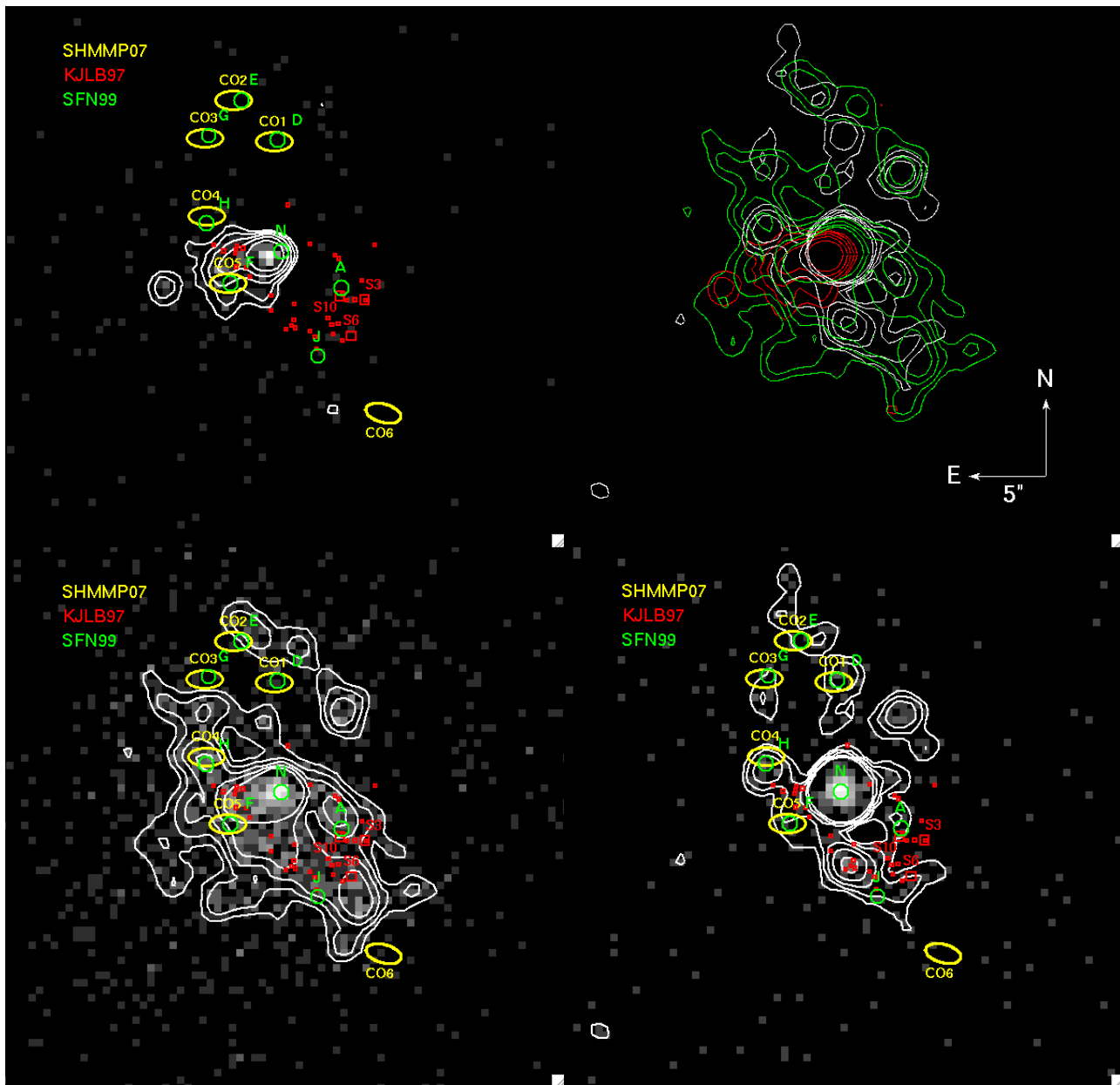


Figure 2. Logarithmically spaced X-ray contours and images during the 2002 *Chandra* observation in the ultrasoft (0.2–0.5 keV; *top left*), the soft (0.5–1.5 keV; *bottom left*), and hard band (1.5–10 keV; *bottom right*). The highest level contours are selected to exclude the AGN point sources in each band, while lowest level contours are selected to exclude background emission. The top right panel overplots the soft (red), medium (green), and hard band (white) emission contours. The circumnuclear star-forming ring of NGC 1365 is also shown here traced by the optical super-star clusters (the SSCs, denoted by red squares; Kristen et al. 1997, KJL97), the radio hotspots (green circles; Stevens et al. 1999, SFN99), and the ^{12}CO molecular hotspots (yellow ellipses; Sakamoto et al. 2007, SHMMP07). The soft band contours are extended in the direction of the radio jet (radio hotspot F), and the [O III] $\lambda 5007$ outflow cone of Hjelm & Lindblad (1996) and Lindblad (1999).

2 THE EXTENDED X-RAY EMISSION OF NGC 1365

2.1 Observation Summary

NGC 1365 was first imaged by *Chandra* in 2002, December. The observation shows diffuse extended nuclear emission in

the inner $20'' \times 20''$ ($\approx 2 \times 2$ kpc) and 23 off-nuclear point sources in the central $\sim 6' \times 6'$ region (Strateva & Komossa 2009, hereafter SK09). Between 2004 and 2006, NGC 1365 was the target of extensive X-ray campaigns which resulted in six additional *Chandra* and five *XMM-Newton* observations (with EPIC-pn exposures of 5.4 ks to 56.5 ks); for more details of the exposure times and dates of these observations, see Table 2. We processed all seven *Chandra* observations with CIAO v.3.4. The 14.6 ks Obs. ID 3554 observation is

Table 1. NGC 1365: X-ray Observation Summary. T_{eff} is the effective exposure time after corrections for flaring and chip position.

ObsID	MJD	T_{eff} [10^3 s]
<i>Chandra</i> 3554	52632	9.9 (ACIS-S3)
<i>Chandra</i> 6871	53835	13.4 (ACIS-S3)
<i>Chandra</i> 6872	53837	14.6 (ACIS-S3)
<i>Chandra</i> 6873	53840	14.6 (ACIS-S3)
<i>Chandra</i> 6868	53843	14.6 (ACIS-S3)
<i>Chandra</i> 6869	53845	14.6 (ACIS-S3)
<i>Chandra</i> 6870	53848	15.5 (ACIS-S3)
XMM 0151370101	52655	14.4 (EPIC pn) 17.6 (MOS)
XMM 0151370201	52679	2.5 (EPIC pn) 5.4 (MOS)
XMM 0151370701	52864	6.6 (EPIC pn) 8.2 (MOS)
XMM 0205590301	53021	49.0 (EPIC pn) 56.5 (MOS)
XMM 0205590401	53210	30.0 (EPIC pn) 44.6 (MOS)

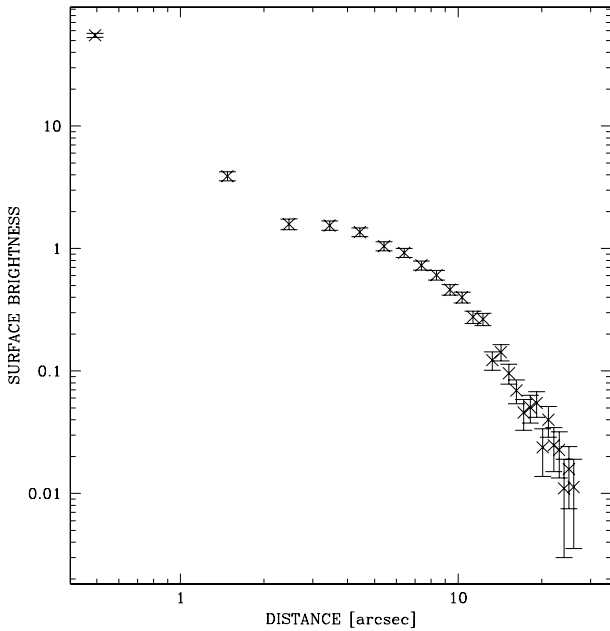


Figure 3. Radial profile of the X-ray emission of NGC 1365 from 2002. The AGN point source is clearly visible in the inner $\sim 1-2''$; the X-ray emission associated with the inner spiral extends to at least $20''$.

reduced to 9.9 ks after the exclusion of a 4.7 ks flare. The remaining 6 *Chandra* observations are free of flaring, with effective times ranging between 13.4 and 15.5 ks.

Using both *Chandra* and *XMM-Newton* we can study in detail the extended emission of NGC 1365, through both spectroscopy and spatially resolved imaging, excluding the absorbed and highly-variable nuclear point source described in detail by e.g., Risaliti et al. (2005a). In this paper we present visual results based on our original 2002 *Chandra* exposure, while using the full *Chandra* and *XMM-Newton* datasets in the analysis.

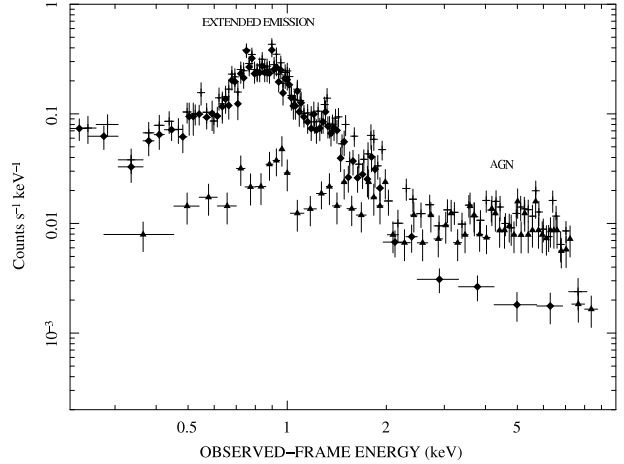


Figure 4. *Chandra* spectra of the AGN point source ($< 2''$; rombs), the extended emission ($2'' < r < 40''$, see text; triangles) and the total emission (crosses). The AGN emission dominates above ~ 2.5 keV, the extended emission dominates below ~ 1.5 keV.

2.2 The Inner Spiral and Outflow Cone of NGC 1365

Kinematically, the nuclear region of NGC 1365 shows two distinct parts: (1) the rotation field of the inner spiral, and (2) the outflowing cone component. The inner spiral is well traced by the optical/infrared (IR) continuum, as well as low excitation lines like the Balmer lines, and the forbidden [N II], [S II], and [O II] lines. The inner spiral has two prominent dust lanes (clearly visible on the HST image in Fig. 1), which can be traced by dense molecular gas, e.g., ammonia (NH_3 ; Ott et al. 2005). The outflowing cone component is traced by higher excitation lines like [O III] $\lambda\lambda 5007, 4958$, [Ne III] $\lambda 3868$, and He II $\lambda 4686$ (Hjelm & Lindblad 1996; Lindblad 1999) and can be seen on Figs. 19 and 22 of Lindblad (1999). Veilleux et al. (2003) constructed a spatially resolved map of the narrow-line-region flux ratios ([O III]/ $\text{H}\beta$ and [N II]/ $\text{H}\alpha$) of the central few kiloparsecs of NGC 1365. They concluded that starburst-like photoionization dominates the nuclear spiral, with the exception of the region associated with the strongest [O III] emission, which, together with the region outside 2 kpc, has the characteristic ratios of AGN photoionization.

2.3 Spatially-Resolved X-ray Emission

The left panel of Figure 1 gives a panoramic view of the NGC 1365 spiral, where we have outlined the nuclear region that we study in detail. The top right panel of Figure 1 shows the 0.3–10 keV X-ray emission contours from the 2002 *Chandra* exposure overlaid on the F555W WFPC2 image of the inner spiral³. The 0.3–10 keV X-ray emission traces well the nuclear spiral component, suggesting that the extended X-ray emission is associated with the circumnuclear starburst ring with projected size $\sim 20'' \times 10''$ (~ 2 kpc \times 1 kpc). The

³ For the multiwavelength comparison we have applied a $\sim 1''$ correction to the X-ray positions requiring that the (> 0.5 keV) X-ray emission peak coincides with the position of the optical emission peak and the radio center N.

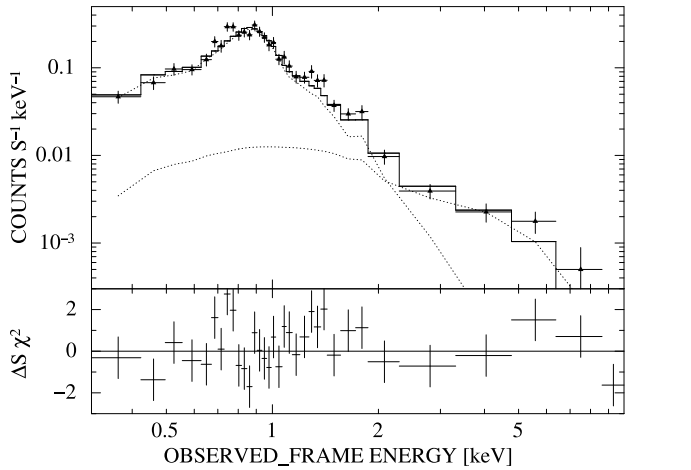


Figure 5. Best fit 0.3–10 keV spectrum for *Chandra* Obs. ID 3554. The model fit includes a thermal plasma (*apec* in XSPEC) with a temperature of ~ 0.7 keV and sub-solar abundance, and a power-law tail with a photon index $\Gamma = 1$. The two model components are shown with dotted lines in the top panel, the fit residuals are shown in a separate panel below.

nuclear starburst ring is traced completely by radio 3 cm and 6 cm emission (Forbes & Norris 1998; Stevens et al. 1999), and partially by molecular CO emission (Sakamoto et al. 2007) and optically detected super-star clusters (SSCs; Kristen et al. 1997), as shown in the bottom right panel of Figure 1.

The spatial distribution of the hard (>1.5 keV) and ultrasoft (<0.5 keV) *Chandra* X-ray photons provide further clues to the origin of the extended X-ray emission. The $2''$ -smoothed X-ray images and contours of the extended emission from the 2002 exposure are presented in Figure 2 in three different energy bands. The 0.2–0.5 keV X-ray emission shown in the upper left panel is not spatially associated with the circumnuclear ring; instead it traces the outflow cone seen in higher optical excitation lines like [O III]. The ultrasoft X-ray emission also coincides with the direction of the probable nuclear jet (extending from the nucleus, N, to radio hotspot F; Stevens et al. 1999), peaking $0.8''$ SW from the centers of the soft- and hard-band emission (which coincide with the radio center N by construction; top right panel of Figure 2). Following the spatial coincidence between the radio, [O III], and ultrasoft X-ray emission, which is confirmed by the emission maps of the remaining 6 *Chandra* observations, we suggest that the ultrasoft emission is either part of an X-ray jet or, more likely, originates in the wide-angle outflow.

The hard (1.5–10 keV) band emission shown in the lower right panel of Figure 2 coincides with some of the radio and molecular hotspots and SSCs. The converse is not true – not all the SSCs have hard X-ray counterparts – the brightest SSCs (S10 and S3), for example, do not correspond to hard X-ray peaks. The general impression on this and the remaining 6 *Chandra* exposures of the same region is that the hard X-rays trace well the circumnuclear starburst ring visible in the optical, radio, and sub-mm. This further suggests that the extended hard X-ray emission is associated with the vigorous nuclear star formation.

The soft (0.5–1.5 keV) X-ray emission is shown in the

bottom left panel of Figure 2. It traces the inner spiral, emphasizing the northern spiral arm in contrast to the adjacent dust lane. The radio hotspots D, E, and G as well as their ^{12}CO molecular counterparts fall within this dust lane and are absorbed in the soft X-rays. The southern spiral arm is much fainter and not visible in the X-ray band, because the NW part of the spiral is nearer to us, while the SE arm is seen absorbed through the galactic plane (see also Figure 1). The soft and hard X-ray emission peaks coincide in Figure 2. Risaliti et al. (2005a, 2007) showed that the hard X-ray emission comes from the central AGN, which is always obscured by a neutral column of at least $\sim 2 \times 10^{23} \text{ cm}^{-2}$. This means that no direct soft X-ray emission is expected from the AGN below 1.5 keV, implying either indirect AGN emission (scattering) or an extra unresolved starburst component which we discuss below. Considering the observed PSF profile shown in Figure 3, the contributions from the wings of the PSF cannot dominate the observed soft emission from the center.

2.4 Chandra spectra of the extended emission

Chandra's spatial resolution allows us to model the extended emission of NGC 1365 by excluding the AGN point source. As can be seen on Figure 3, which shows the radial profile of NGC 1365 during Obs. ID 3554, the AGN point source dominates the emission from the inner $\sim 2''$, which we excluded from the following analysis. Figure 4 shows the *Chandra* 2002 spectra extracted from the inner $2''$, a $40''$ circular annulus excluding the inner $2''$ (the extended emission), and the total emission within $40''$. The emission above ~ 3 keV is clearly dominated by the active nucleus, that below ~ 1.5 keV – by the extended emission, as already noted by Risaliti et al. (2005a). The extended emission peaks around 0.7–0.8 keV, which suggest a thermal-plasma emission origin.

After experimenting with a few different thermal-plasma models (XSPEC models *mekal*, *cmekal*, *apec*, *raymond*, etc.), we find that *apec* models the thermal emission best, but the differences are not significant.⁴ In the full 0.3–10 keV *Chandra* band, in addition to the thermal-plasma component, there is an extended power-law emission tail above 2 keV. Using the 2–10 keV extended-emission spectrum, we determined a best-fit photon index of $\Gamma = 1.1 \pm 0.5$ in ObsID 3554, which is substantially different from that of the AGN in the 2–10 keV band, whose simple power law slope is $\Gamma \approx -0.8$; this suggests that the extra component is not dominated by emission from the AGN.⁵ The addition of the power-law component significantly improves the 0.3–10 keV fits, with F-test probability of 10^{-8} . The best fit 0.3–10 keV spectral model including the thermal

⁴ All models include absorption equal to the Galactic value of $1.4 \times 10^{20} \text{ cm}^{-2}$.

⁵ In our original 2002 observation, the extended emission counts in the 2–10 keV (5–10 keV) band are equal to about 28% (56%) of the total AGN counts in the same band, while the expected contamination from the wings of the PSF should be about 10%. In the subsequent *Chandra* observations, when the AGN was more luminous, the contamination is stronger, especially around and above 5 keV, which is also confirmed by comparing the hard-band spectral slope of the extended emission with that of the AGN.

Table 2. NGC 1365 0.3–1.5 keV emission: Fluxes and Spectroscopic Fits. All model fits include a cold absorber equal to the Galactic value of $1.4 \times 10^{20} \text{ cm}^{-2}$; the second fit to ObsID 3554 includes intrinsic absorption of $(7 \pm 2) \times 10^{20} \text{ cm}^{-2}$. The fluxes are quoted in units of $10^{-13} \text{ erg s}^{-1} \text{ cm}^{-2}$ and all *XMM-Newton* fluxes are scaled by 20% to account for the AGN contribution. All errors are 90% confidence limits; fit parameters given in parenthesis were held fixed during the fit. Approximate values are given for parameters which were unconstrained by the fit.

ObsID	Counts	model	$F_{0.3-1.5 \text{ keV}}$	Γ	kT_1 [keV]	Z_1/Z_\odot	kT_2 [keV]	Z_2/Z_\odot	χ^2/DoF
3554	1591	<i>apec+zpow</i>	$5.3^{+0.6}_{-1.1}$	(1)	0.65 ± 0.03	0.17 ± 0.04	48/54
6871	2006	<i>apec+zpow</i>	$5.4^{+0.5}_{-1.1}$	(1)	0.64 ± 0.02	0.16 ± 0.03	43/46
6872	2276	<i>apec+zpow</i>	$5.5^{+0.7}_{-1.4}$	(1)	0.64 ± 0.02	0.21 ± 0.02	50/56
6873	2182	<i>apec+zpow</i>	$5.2^{+0.5}_{-1.4}$	(1)	0.65 ± 0.03	0.16 ± 0.04	77/55
6868	2221	<i>apec+zpow</i>	$5.4^{+0.6}_{-1.0}$	(1)	0.71 ± 0.03	0.15 ± 0.03	69/59
6869	2366	<i>apec+zpow</i>	$5.4^{+0.5}_{-1.3}$	(1)	0.63 ± 0.02	0.20 ± 0.04	83/55
6870	2193	<i>apec+zpow</i>	$5.5^{+0.5}_{-0.9}$	(1)	0.62 ± 0.02	0.15 ± 0.03	66/53
0151370101	9167	<i>apec+zpow</i>	$6.5^{+0.3}_{-0.3}$	(1)	0.66 ± 0.01	0.10 ± 0.01	348/318
0151370201	2080	<i>apec+zpow</i>	$6.6^{+0.8}_{-0.9}$	(1)	0.70 ± 0.03	0.09 ± 0.01	96/87
0151370701	4575	<i>apec+zpow</i>	$6.8^{+0.4}_{-0.3}$	(1)	0.71 ± 0.01	0.10 ± 0.01	191/175
0205590301	35873	<i>apec+zpow</i>	$6.8^{+0.2}_{-0.1}$	(1)	0.64 ± 0.01	0.096 ± 0.004	702/626
0205590401	22517	<i>apec+zpow</i>	$6.8^{+0.3}_{-0.4}$	1.0 ± 0.5	0.64 ± 0.01	0.10 ± 0.01	542/468
3554	1591	<i>zwabs*apec</i>	$7.7^{+0.6}_{-1.3}$...	0.66 ± 0.03	0.07 ± 0.01	52/54
6871	2006	<i>apec+apec</i>	$5.5^{+0.4}_{-0.8}$...	1.2 ± 0.2	0.06 ± 0.03	0.61 ± 0.04	(1)	38/45
6872	2276	<i>apec+apec</i>	$5.4^{+0.4}_{-0.4}$...	1.0 ± 0.1	(0.1)	0.55 ± 0.04	(1)	60/56
6873	2182	<i>apec+apec</i>	$5.4^{+0.4}_{-0.7}$...	0.99 ± 0.07	0.10 ± 0.02	0.54 ± 0.07	(1)	63/54
6868	2221	<i>apec+apec</i>	$5.4^{+0.6}_{-0.6}$...	1.7 ± 0.4	0.70 ± 0.03	0.70 ± 0.03	(1)	68/58
6869	2366	<i>apec+apec</i>	$5.4^{+0.5}_{-0.7}$...	1.2 ± 0.2	0.10 ± 0.03	0.58 ± 0.04	(1)	73/54
6870	2193	<i>apec+apec</i>	$5.4^{+0.7}_{-0.7}$...	1.2 ± 0.2	$\lesssim 0.1$	0.62 ± 0.03	(1)	68/52
0151370101	9167	<i>apec+apec</i>	$6.6^{+0.4}_{-0.2}$...	1.5 ± 0.1	$\lesssim 0.02$	0.66 ± 0.01	(1)	350/317
0151370201	2080	<i>apec+apec</i>	$6.7^{+0.6}_{-0.7}$...	1.3 ± 0.2	$\lesssim 0.02$	0.66 ± 0.03	(1)	99/86
0151370701	4575	<i>apec+apec</i>	$6.7^{+0.4}_{-0.5}$...	1.1 ± 0.1	0.02 ± 0.01	0.66 ± 0.02	(1)	190/174
0205590301	35873	<i>apec+apec</i>	$7.3^{+0.2}_{-0.1}$...	1.7 ± 0.1	$\lesssim 0.02$	0.64 ± 0.01	(1)	724/625
0205590401	22517	<i>apec+apec</i>	$6.9^{+0.1}_{-0.2}$...	1.15 ± 0.05	0.020 ± 0.005	0.62 ± 0.01	(1)	547/468

plasma and power-law emission components for *Chandra* ObsID 3554 is shown in Figure 5. The 0.3–10 keV luminosities of each of the two components are: $3.0^{+1.1}_{-0.2} \times 10^{40} \text{ erg s}^{-1}$ for the thermal component and $1.8^{+0.9}_{-1.1} \times 10^{40} \text{ erg s}^{-1}$ for the power-law component. As noted above, the thermal plasma dominates the soft-band extended emission; in the 2–10 keV band the power law model contributes $1.4^{+0.4}_{-1.3} \times 10^{40} \text{ erg s}^{-1}$ to the extended emission, while the thermal plasma only $\sim 1.3 \times 10^{39} \text{ erg s}^{-1}$.

For some of the remaining *Chandra* observations, e.g. ObsID 6868, the 2–10 keV emission seems to be contaminated by the AGN even beyond $2''$ from the center, as evidenced by the 2–10 keV power law photon index of $\Gamma \approx -0.5$, the large ratio between AGN and extended-emission counts around 5 keV, and the residuals between 6 and 7 keV (which are consistent with an Fe-K α origin). Consequently, we restrict our analysis to the 0.3–1.5 keV band, which, as shown above both spatially and spectroscopically, is dominated by the extended emission, even for the case of the much lower spatial resolution *XMM-Newton* data. Table 2.4 lists the total counts and thermal plasma model fit parameters obtained in the soft band for all seven *Chandra* observations. The single temperature thermal plasma model provides a poor fit to the 0.3–1.5 keV data in all cases, and we consider the addition of a power law or a two-temperature plasma model instead. Both models provide significant improvements of the spectral fits (F-test probabilities of $< 0.1\%$) and in most cases the current data does not show a clear

preference for either of the two models. For the thermal plasma plus power-law model results shown in the top part of Table 2.4, we fix the power law slope to $\Gamma = 1$, the value found in the 2–10 keV *Chandra* fits unaffected by the AGN. This slope is confirmed in the soft band fit to the longest *XMM-Newton* observation, as discussed below. An example *Chandra* 0.3–1.5 keV spectral fit from the upper part of Table 2.4 (Obs. ID 6870) is shown in Figure 6.

Overall the *Chandra* spectra of NGC 1365 suggest a thermal plasma extended emission origin for the soft X-ray emission, with additional contribution from a second temperature thermal plasma or a $\Gamma = 1$ power law. The fitted abundances in Table 2.4 are sub-solar, inconsistent with our general ideas about the recycling of materials around AGNs and the abundance measurements and gradients of NGC 1365 (e.g., Galliano et al. 2005 report central abundance of 3 times solar). Sub-solar abundances are commonly found when applying simple thermal plasma models (e.g., Buote & Fabian 1998), and are considered a sign of the model simplifications (e.g. thermal equilibrium vs. shocks, etc.).

From Figure 4, the spectrum of the inner $2''$ emission has a low flux soft X-ray component extending below 2.5 keV. As noted in § 2.3, this unresolved core emission in the soft band is unlikely to originate directly from the active nucleus, which is absorbed by a large neutral column. The 0.3–1.5 keV core (within $2''$) emission can be represented by a spectral model including thermal plasma

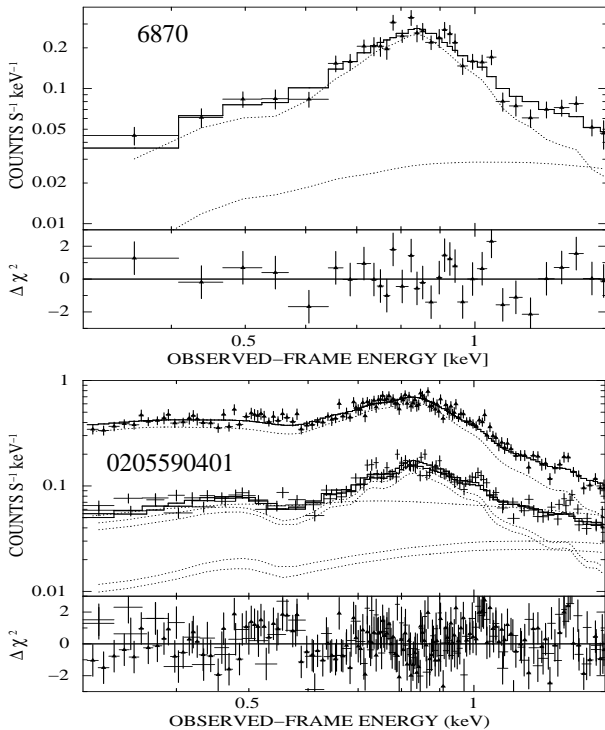


Figure 6. Best fit 0.3–1.5 keV spectra for an example *Chandra* (Obs. ID 6870, top) and *XMM-Newton* (Obs. ID 0205590401, bottom) observation. The model fits include a thermal plasma (*apec* in XSPEC) with a temperature of ~ 0.62 keV, and a power-law tail with a photon index $\Gamma = 1$. The model fit components are shown separately with dotted lines below the fit; the fit residuals are shown in the lower panel.

($kT = 0.8 \pm 0.1$ keV and abundances fixed to 0.17 of solar) and a power law absorbed by a Galactic neutral absorber consistent with the model fit of the extended emission. The luminosity of this core component is low – $L_{0.3-1.5 \text{ keV}} = 4.4 \pm 1.1 \times 10^{39}$ ergs s^{-1} , $\approx 15 \pm 5\%$ of the 0.3–1.5 keV band luminosity of the extended emission, too large to be attributed to the PSF wings of the extended emission surrounding the center. Based on the similarity of the spectral shape of this core component to that of the extended star-formation associated emission, we speculate that this soft X-ray core component is dominated by unresolved recent star formation in the immediate vicinity of the active nucleus.

2.5 XMM-Newton spectra of the extended emission

Due to the fact that the soft emission is dominated by the extended component of NGC 1365 and the heavily obscured AGN’s contribution is expected to be negligible below 1.5 keV, we can use the 0.3–1.5 keV *XMM-Newton* observations of NGC 1365 to constrain the properties of the extended emission. The unresolved soft X-ray emission component found within $2''$ of the active nucleus in the *Chandra* observation above, has identical 0.3–1.5 keV spectrum and will only increase the total flux by about 15%. In each case we extract the 0.3–1.5 keV *XMM-Newton* spectrum from a $40''$ region centered on NGC 1365 and bin it to >20 counts per bin in order to use χ^2 minimization fitting

in XSPEC. The corresponding *XMM-Newton* spectral fits are given in Table 2.4, together with the *Chandra* fits for comparison. The quoted fluxes are *XMM-Newton pn* fluxes. Note that they are about 20% brighter than the corresponding *Chandra* fluxes, in agreement with the expected soft-band contribution of the unresolved core emission. The 0.3–1.5 keV *XMM-Newton* spectra are well represented by the thermal plasma plus power-law model found in the *Chandra* fits, with the exception of the two longest observations, ObsID 0205590301 and ObsID 0205590401, where this fit is inadequate ($\chi^2/DoF=702/625$ and $\chi^2/DoF=542/468$, respectively). Adopting varying abundances for some elements (e.g. Fe, Mg, Si, He) provides acceptable fits in both cases ($\chi^2/DoF=663/621$ and $\chi^2/DoF=514/464$), but considering the simplicity of the one-temperature collisionally ionized diffuse gas models, the caveats associated with the *apec* and *mekal* models in XSPEC, and the inconsistencies and poor constraints on the fitted abundance values of these model fits, we refrain from interpreting these abundance variations here. Wang et al. (2009) suggest that allowing element abundances to vary independently for different spatial regions can resolve the problem of the small fitted overall abundance.

We checked the longest *XMM-Newton* observation for variability in the soft band (0.3–1.5 keV) on timescales of hours, but found no significant variation.

3 DISCUSSION AND CONCLUSIONS

3.1 Multiwavelength View of the Nuclear Spiral

The spatially-resolved 0.5–10 keV emission of NGC 1365 traces well the nuclear spiral component, suggesting that the extended X-ray emission is associated with the circum-nuclear starburst. This is confirmed by the spatially resolved *Chandra* spectroscopy, which, together with the unresolved *XMM-Newton* soft-band spectra, are dominated by thermal plasma emission with temperature ~ 0.7 keV. The ultrasoft X-ray emission (<0.5 keV), on the other hand, is confined to the outflow cone seen by Hjelm & Lindblad (1996), Lindblad (1999), and Veilleux et al. (2003) in the kinematic signature of the high excitation optical emission lines. Soft-X-ray emission associated with a NLR outflow has been seen before, notably in NGC 4151 and NGC 1068, where the outflows are photoionized and photoexcited by the AGN (e.g., Ogle et al. 2000, 2003; Schurch et al. 2004). In the case of NGC 1365, Veilleux et al. (2003) show that the optical narrow-line ratios associated with the outflow cone are consistent with AGN photoionization outside the nuclear spiral region, but have the photoionization characteristics of a starburst inside the inner 1–2 kpc. In fact, as we argue below, the NGC 1365 starburst is powerful enough to drive a strong outflow like the one observed.

The molecular starburst ring of NGC 1365 is defined in the radio band, by radio 3 cm and 6 cm emission (Forbes & Norris 1998; Stevens et al. 1999) and well traced in the MIR by *Spitzer*, as well as by the string of super-star clusters in the optical (SSCs; Kristen et al. 1997). There is evidence for molecular gas in the center which is dense ($\gtrsim 10^4 \text{ cm}^{-3}$) and cold (kinetic temperature of 40 K for NGC 1365; Ott et al. 2005), traced by NH_3 , which correlates

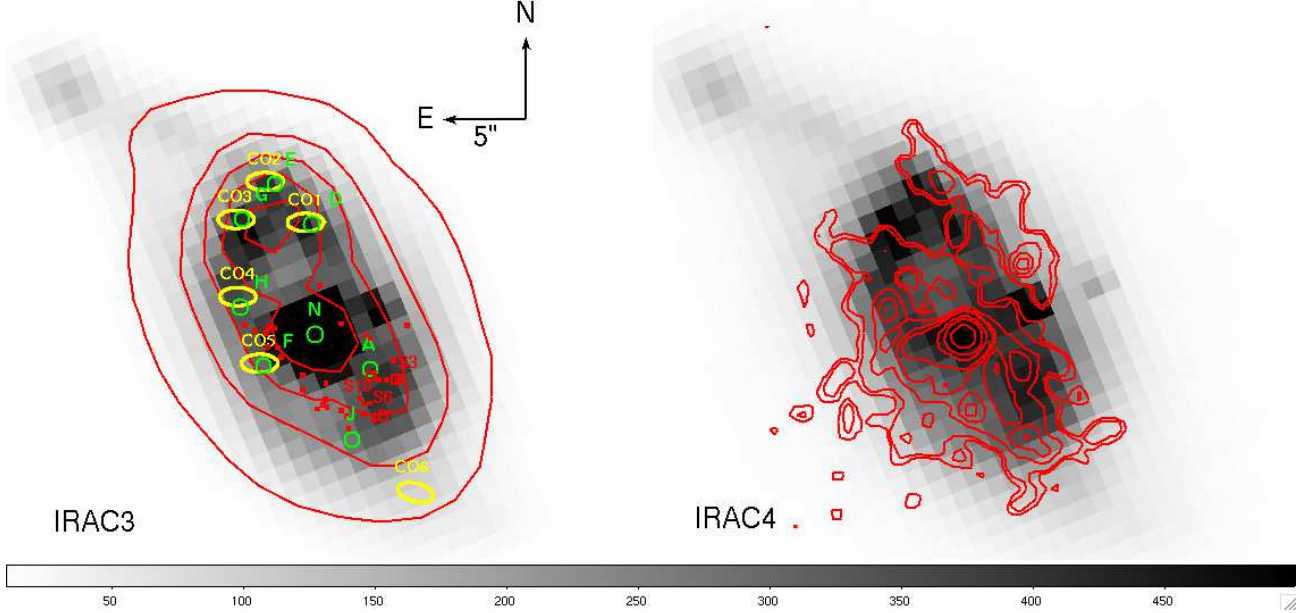


Figure 7. *Spitzer* IRAC3 ($5.8 \mu\text{m}$, left) and IRAC4 ($8.0 \mu\text{m}$, right) images of the nuclear starburst ring. The central nuclear emission dominates at and below $\sim 6 \mu\text{m}$; the circumnuclear starburst ring emission is comparable at $8 \mu\text{m}$, and dominates the IR emission at longer wavelengths, for example, the $24 \mu\text{m}$ MIPS emission shown in the left panel as contours. The right panel displays also the 0.3–10 keV *Chandra* contours (from Obs. ID 3554). The super-star clusters, radio hotspots, and ^{12}CO molecular hotspots of the nuclear starburst ring are shown in the right panel with symbols following those of Figure 1.

well with other star-formation indicators. The CO emission maps of Sakamoto et al. (2007) confirm the presence of less dense molecular gas, with the ^{12}CO and ^{13}CO molecular maps tracing the circumnuclear ring structure dotted by emission hotspots.

NGC 1365 was recently imaged with *Spitzer* with both IRAC and MIPS (Brandl et al. 2006). Figure 7 shows the $5.8 \mu\text{m}$ and $8 \mu\text{m}$ IRAC images together with the $24 \mu\text{m}$ MIPS (left panel) and the 0.3–10 keV X-ray (right) contours, as well as the circumnuclear ring SSCs, radio, and molecular CO hotspots. The circumnuclear star forming ring is traceable in the MIR in both panels, gaining prominence with respect to the nuclear component at $8 \mu\text{m}$. At shorter MIR wavelengths the nuclear point source dominates the emission, at wavelengths increasingly longer than $8 \mu\text{m}$ the starburst dominates. The $24 \mu\text{m}$ MIPS emission contours shown in Figure 7 peak in the NW-running dust lane, where the X-ray emission is mostly absorbed in the *Chandra* band, but the molecular ^{12}CO emission (CO1, CO2, and CO3 in Figure 7) and the radio emission (hotspots D, E, and G) are strong. We address the nature of the emission in this strong MIR emission region in the next section.

The (spatially unresolved) $5\text{--}38 \mu\text{m}$ spectrum of NGC 1365 is a fairly shallow power law with no evidence of silicate absorption and weak 6.2, 7.7, 8.6, and $11.3 \mu\text{m}$ polycyclic aromatic hydrocarbon (PAH) features. The starburst dominates, but a prominent AGN component must also be present, and overall the nucleus lies (fully on the starburst side but) close to the line separating starbursts and AGN on the MIR-slope diagnostic of Brandl et al. (2006). Using our assumed distance of 21 Mpc and the *Spitzer* the

$15 \mu\text{m}$ and $30 \mu\text{m}$ *Spitzer* fluxes (Brandl et al. 2006), the MIR SFR estimate is $\text{SFR}_{\text{Spitzer}} \approx 9 M_{\odot} \text{yr}^{-1}$. This is about 25% smaller than the FIR-estimated global NGC 1365 SFR, which is $\text{SFR}_{\text{FIR}} \approx 12 M_{\odot} \text{yr}^{-1}$, if we assume the Lonsdale et al. 1985 $L_{\text{FIR}} = 6.8 \times 10^{10} L_{\odot}$ measurement and eqn. 3 of Kennicutt (1998).

The soft-band X-ray luminosity can also be used to estimate of the star-formation rate. With the help of eqn. 14 of Ranalli et al. (2003), $\text{SFR} = 2.2 \times 10^{-40} L_{0.5-2 \text{keV}} M_{\odot} \text{yr}^{-1}$, and the observed 0.5–2 keV luminosity of the extended emission, $L_{0.5-2 \text{keV}} = 3 - 3.6 \times 10^{40} \text{ergs s}^{-1}$ (where the higher value includes the contribution of an unresolved starburst component within $2''$ from the AGN), we estimate a soft-X-ray of $\text{SFR}_{0.5-2 \text{keV}} = 7 - 8 M_{\odot} \text{yr}^{-1}$. This is in good agreement (10–20% lower) than the *Spitzer* nuclear SFR estimate, which covers a slightly larger area, and about 30–40% lower than the global FIR-estimated SFR. We conclude that most of the strong star formation (60–70% or $7\text{--}8 M_{\odot} \text{yr}^{-1}$) is constrained to the nuclear starburst ring in the inner region of NGC 1365.

3.2 Radio hotspots, Super-Star Clusters and Molecular clouds

Radio hotspots A, D, G, and H have flat, non-thermal spectra between 6 and 20 cm (Sandqvist et al. 1995). Sandqvist et al. (1995) suggest that radio hotspots A, D, and G (A and G are unresolved at 2 cm, while D is only marginally detected) are related to the star formation and supernova activity. Radio hotspots D and G (which coincide with CO hotspots CO1 and CO3) fall within the

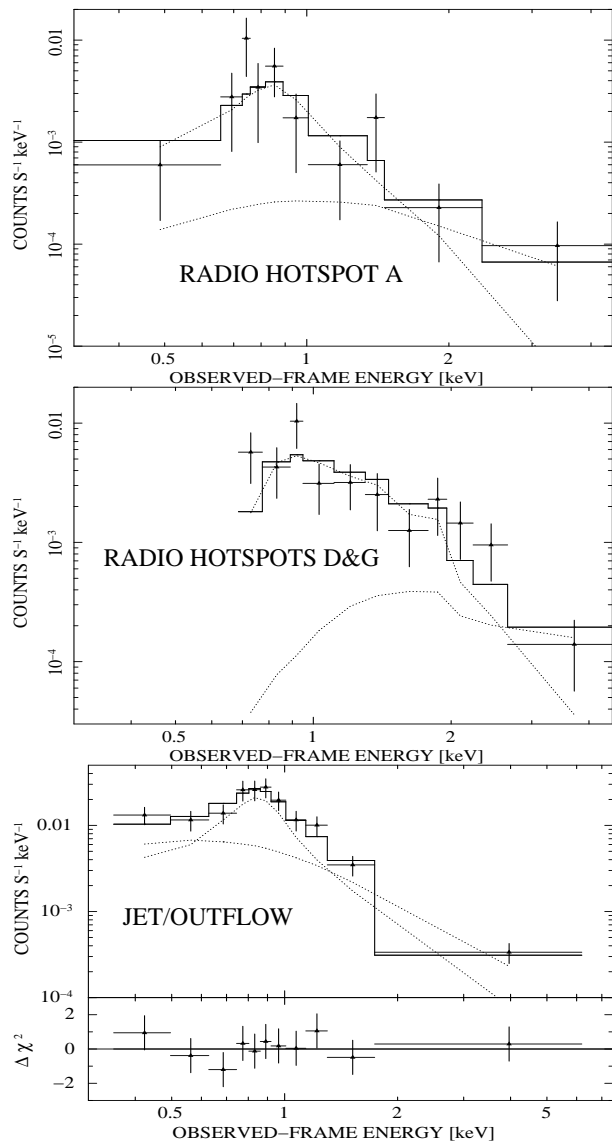


Figure 8. X-ray spectra of select multi-wavelength counterparts for *Chandra* Obs. ID 3554: the radio-hotspot A (SSC10; *top panel*), radio hotspots D & G (*middle panel*), and radio hotspot F (jet/high-ionization outflow; *bottom panel*).

prominent dark NW dust lane, and are associated with two obscured star-forming regions detected in the infrared by Moorwood et al. (1998) and visible in the IRAC image of NGC 1365 shown in Brandl et al. (2006) and our Figure 7. Galliano et al. (2005) and Sakamoto et al. (2007) suggest that the MIR peaks associated with radio hotspots D, E, and G (M4, M5, and M6 in Galliano et al. 2005, 2008) correspond to SSCs. Using VLT images and spectra Galliano et al. (2008) revised the mass and age estimates of earlier works to show that the superstar clusters in NGC 1365 are the most massive clusters found so far, with masses of at least $10^7 M_{\odot}$ and ages of ~ 7 Myr. These SSCs are still embedded in large amounts of gas and dust due to dust trapping, unlike typical lower-mass star clusters found in less dense environments which sweep away their gaseous/dusty envelopes much earlier.

Using the X-ray images we can obtain estimates of the

X-ray radiation from the radio and ^{12}CO hotspots and the HST SSCs. X-ray spectra extracted from $1''$ -regions⁶ around the radio positions of sources D and G have only a handful of counts (16–24), but are consistent with the *apec+zpov* (or simple *apec*) models with parameters fixed to those reported in Table 2.4 for each *Chandra* observation, if we also include an intrinsic absorber with column density of $\sim 0.5 - 1 \times 10^{22} \text{ cm}^{-2}$ (see the middle panel of Fig. 8). The unabsorbed luminosity estimates for the 0.3–10 keV band correspond to $L_x \sim 1 - 3 \times 10^{39} \text{ erg s}^{-1}$ for both radio hotspots taken together. These luminosities are in agreement with the theoretical predictions for the highest mass clusters ($10^6 M_{\odot}$) studied by Silich et al. (2005), which have $L_x \sim 1 - 10 \times 10^{39} \text{ erg s}^{-1}$ (depending on the density of the surrounding interstellar medium, the gas metallicity, etc.), but these predictions do not take into account the effects of gas-trapping in heavier clusters, which is likely relevant for the SSCs behind radio hotspots D and G.

Radio hotspot A, which has no molecular ^{12}CO equivalent, falls in an optically and X-ray unabsorbed region and is likely associated with a super-star cluster SSC10 identified by Kristen et al. (1997) (Stevens et al. 1999). There are 15–39 counts within $1''$ of the optical (similar for the slightly offset radio) positions in the different *Chandra* observations and *apec+zpov* Cash statistic model fits with parameters fixed to those of the extended *Chandra* emission fits from Table 2.4 and free normalization provide acceptable fits in all cases (see the top panel of Fig. 8 for an example). The inferred 0.3–10 keV $1''$ flux is $L_x \sim 6 - 10 \times 10^{38} \text{ erg s}^{-1}$. The B-band and radio luminosities of SSC10 are $L_B = 4.2 \times 10^{39} \text{ erg s}^{-1}$ and $L_{3 \text{ cm}} = 5.2 \times 10^{36} \text{ erg s}^{-1}$, the corresponding ratios $L_x/L_B \sim 0.1 - 0.2$ and $L_{3 \text{ cm}}/L_x \sim 0.005 - 0.009$.

Radio hotspot F (which coincides with CO5) is traditionally identified with a radio jet (Sandqvist et al. 1995; Stevens et al. 1999). We argued above, that the ultrasoft X-ray emission is associated with the outflow cone seen in higher excitation lines like [O III] and [Ne III] (Hjelm & Lindblad 1996; Lindblad 1999). We extracted X-ray spectra from the region between radio hotspots N and F, which overlaps with the ultrasoft emission contours shown in Figure 2, for each of the *Chandra* pointings, excluding the $2''$ -radius around the center which is affected by the AGN. The spectra can be fit by *apec+zpov* models, with the *apec* model parameters fixed to these quoted in Table 2.4 as shown in the bottom panel of Fig. 8. Unlike the case of the overall extended emission component however, the power-law component dominates the X-ray spectrum of the outflow at both high and low energies, i.e. the power-law index is much steeper – typically $\Gamma \sim 2.5$ – and the normalization of this component much higher. The *apec+zpov* fits (including absorption equal to the Galactic value in all cases) are acceptable in most cases, but the residuals show excess emission below 0.5 keV, i.e. the ultrasoft emission seen in Figure 2 is not fully accounted for by the steeper power-law. The lower limit to the energy (since we exclude the highest surface brightness inner region due to AGN contamination) in the 0.3–10 keV band for this outflow is $L_{x,\text{jet}} \gtrsim 4 \times 10^{39} \text{ erg s}^{-1}$.

⁶ For *Chandra* on-axis observations, 80–90% of the total energy falls in a circle with radius $\sim 1''$.

3.3 Starburst-Driven Superwind

Starburst-driven superwinds (as well as AGN driven outflows) can explain the extended, often biconical, X-ray emission in nearby galaxies (e.g., Heckman et al. 1996; Komossa & Schulz 1998). Komossa & Schulz (1998) concluded that the extended soft X-ray emission observed in NGC 1365 could be the result of a starburst driven wind. We repeat the Komossa & Schulz (1998) estimates here, using the new data on the SFR and new supernova (SN) rate estimates, assuming a velocity of $\sim 100\text{--}200 \text{ km s}^{-1}$ on $\sim 1\text{--}2 \text{ kpc}$ scales.

We use two different methods to obtain an estimate of the SN rate. Cappellaro & Turatto (2001) tabulate the expected SN rates as a function of B-band luminosity and the galaxy type. The B-band luminosity of NGC 1365 is $7.9 \times 10^{10} L_{\odot}$ (see Table 2 of Sandqvist et al. 1988), resulting in a SN rate of 0.09 yr^{-1} . Using the FIR luminosity method, we obtain slightly higher SN rate in the range $0.14\text{--}0.16 \text{ yr}^{-1}$ (van Buren & Greenhouse 1994; Mannucci et al. 2003). Both the B-band and the FIR-luminosity SN rate estimates apply to the whole galaxy. Scaling the global SN rate by assuming that 60–70% of the new stars and SN are born in the inner spiral, we arrive at a central SN rate in the range $0.05\text{--}0.1 \text{ yr}^{-1}$. For comparison the radio-band inferred SN rate reported by Stevens et al. (1999) is about $0.02\text{--}0.03 \text{ yr}^{-1}$ over a smaller ($\sim 1 \text{ kpc}^2$) area including the central $\sim 0.6 \text{ kpc}$.

Following Komossa & Schulz (1998), the mechanical power or a starburst driven wind in NGC 1365 is $L_{\text{mech}} \approx 1 - 3 \times 10^{42} \text{ erg s}^{-1}$, assuming each supernova gives $L_{\text{SN}} = 10^{51} \text{ erg yr}^{-1}$. With a soft-band luminosity of $L_{0.1\text{--}2.4 \text{ keV}} = 4.4 \times 10^{40} \text{ erg s}^{-1}$, the Komossa & Schulz (1998) estimates (their eqns. 1 through 3, based on Heckman et al. 1996) still hold, if we assume a mean density of the swept-up interstellar medium in the range $n = 0.1 - 1 \text{ cm}^{-3}$ for an outflow velocity of $\sim 100\text{--}200 \text{ km s}^{-1}$ on $\sim 1\text{--}2 \text{ kpc}$ scales. Therefore the observed starburst could supply the observed thermal X-rays in a wind driven shell.

The $\text{H}\alpha$ emission expected for a SFR of $\sim 7\text{--}8 M_{\odot} \text{ yr}^{-1}$ is $\sim 10^{42} \text{ erg s}^{-1}$ (Kennicutt 1998) much larger than the $\text{H}\alpha$ luminosity observed by Kristen et al. (1997): $8 \times 10^{40} \text{ erg s}^{-1}$ (converted to a distance of 21 Mpc) for the two most luminous $\text{H}\alpha$ hotspots located SW of the nucleus (in the region of the HST-detected SSCs shown in Figures 1, 2, and 7). The total extended $\text{H}\alpha$ luminosity likely exceeds this estimate by a factor of a few. Considering the large obscuration inferred towards the star-formation regions in the NE of the nucleus (for example, those associated with radio hotspots D, and G, which are optically faint, but infrared and radio bright, hidden behind $N_H \approx 10^{22} \text{ cm}^{-2}$ according to the X-ray emission), it is conceivable that as little as $\sim 10\%$ of the $\text{H}\alpha$ luminosity associated with the vigorous star formation is observed directly.

3.4 AGN contribution and IR-Optical-X-ray relations

Komossa & Schulz (1998) considered the place of the NGC 1365 AGN among the IR-Optical-X-ray relations found by Ward et al. (1988) for the sample of Piccinotti et al. (1982). They concluded the AGN was too

faint in the X-rays relative to the luminosity expected based on the observed broad $\text{H}\alpha$ -line emission and the total IR emission. We know now that the AGN luminosity in the 2–10 keV band, based on the Iyomoto et al. (1997) fit to the ASCA data, was underestimated, and that in the Compton thin state, the AGN absorption-corrected luminosity is about an order of magnitude higher, $L_{\text{AGN},2\text{--}10 \text{ keV}} = 0.8 - 1.7 \times 10^{42} \text{ erg s}^{-1}$ (Risaliti et al. 2005a, 2007). The value expected for the hard-band X-ray luminosity based on the broad-line $\text{H}\alpha$ luminosity observed by Schulz et al. (1994), is $L_{\text{AGN},2\text{--}10 \text{ keV}} \approx 0.6 \times 10^{42} \text{ erg s}^{-1}$ (corrected to a distance of 21 Mpc), comparable to the lower range of the observed hard-band AGN emission.

Using the IR continuum fluxes at $15 \mu\text{m}$ and $30 \mu\text{m}$ given by Brandl et al. (2006, see their Table 3), we estimate $L_{25\text{--}60 \mu\text{m}} = 2.3 \times 10^{44} \text{ erg s}^{-1}$ (as in Ward et al. 1988, including setting $H_0 = 50 \text{ km s}^{-1} \text{ Mpc}^{-1}$ for the comparison). The expected hard-band X-ray luminosities is then a factor of 10–20 higher than the Risaliti et al. (2005b) observations. We believe this discrepancy is primarily due to the fact that the starburst dominates the IR emission beyond $6\text{--}15 \mu\text{m}$, while the Ward et al. (1988) relations refer to the hard-band X-ray and IR emission of the AGN. According to Ward et al. (1988), the IR emission from the AGN component is NGC 1365 should be $L_{25\text{--}60 \mu\text{m}} \lesssim 2 \times 10^{43} \text{ erg s}^{-1}$. If the AGN dominates the emission at and below $6 \mu\text{m}$, the $6 \mu\text{m}$ flux density should be a better predictor of the AGN hard-band flux. This is indeed the case. The average ratio of the $6 \mu\text{m}$ flux density to the 2–10 keV flux for type 2 AGNs was found to be $\log[F_{2\text{--}10 \text{ keV}}/\nu F_{\nu}(6 \mu\text{m})] = -0.61$ by Lutz et al. (2004), in agreement with the values observed for NGC 1365: $-0.9 \leq \log[F_{2\text{--}10 \text{ keV}}/\nu F_{\nu}(6 \mu\text{m})] \leq -0.6$.

4 SUMMARY

Using *Chandra*'s excellent spatial resolution and *XMM-Newton*'s higher photon gathering capabilities we study the extended nuclear emission of the supergiant barred galaxy NGC 1365. The combination of radio, infrared, optical and X-ray data reveals the complex structure of the nuclear region (within about a kiloparsec of the center) highlighting the competing effects of the AGN, the circumnuclear starburst ring, and the central outflow.

The ultrasoft X-ray emission (below $\sim 0.5 \text{ keV}$) is spatially coincident with the AGN-driven outflow cone traced by higher excitation optical emission lines (Hjelm & Lindblad 1996; Lindblad 1999; Veilleux et al. 2003). The X-ray spectrum of the outflow region can be represented by a dominant steep ($\Gamma \approx 2\text{--}3$) power-law component; the steepness of the power law is driven by the excess emission below $\sim 0.5 \text{ keV}$.

Spectroscopic as well as spatial evidence suggests that the soft X-ray emission (0.5–1.5 keV) of NGC 1365 has thermal origin related to the $\sim 1 \text{ kpc}$ -radius circumnuclear starburst. Thermal plasma emission models can fit the *Chandra* and *XMM-Newton* spectra well, with $kT \sim 0.6\text{--}0.7 \text{ keV}$; a second thermal component with $kT \sim 1.3 \text{ keV}$ or a power-law with $\Gamma \approx 1$ is also necessary to fit the observed spectra. Considering the high star-formation rate in the nuclear region ($\sim 7\text{--}8 M_{\odot} \text{ yr}^{-1}$) and the associated high SN rates, a starburst-driven superwind is likely present, and can account

for the wide angle outflow observed in the higher excitation optical emission lines and the ultrasoft X-rays.

The hard X-ray emission beyond ~ 2 keV is dominated by the obscured AGN, which also contributes substantially to the infrared emission below $\sim 6\text{--}15\ \mu\text{m}$. The circumnuclear ring is also traced by low-surface brightness hard X-ray emission, suggesting that an obscuring column of $\approx 10^{22}\ \text{cm}^{-2}$ is hiding the ~ 7 Myr old (but still shrouded in gas and dust) $\sim 10^7 M_{\odot}$ super-star clusters seen in the radio, molecular CO, and mid-infrared in the NE part of the nuclear starburst ring from view in the optical and soft X-ray bands.

The central regions of NGC 1365 are influenced by the strong bar and nuclear spiral, which channel sufficient material to the innermost regions and are likely responsible for the circumnuclear starburst as well as fueling the super-massive black hole. Overall, the extended emission (which also contains unresolved point sources) contributes about $5 \times 10^{40}\ \text{erg s}^{-1}$ in the *Chandra* X-ray band, similar to the total emission from X-ray point sources (Strateva & Komossa 2009) during the 2002 *Chandra* observation. The AGN is an order of magnitude more powerful ($1 - 2 \times 10^{42}\ \text{erg s}^{-1}$) than the combined extended plus point source emission ($\sim 10^{41}\ \text{erg s}^{-1}$), but $\sim 70\%$ of this emission is obscured by gas in the immediate vicinity of the active nucleus, which is associated with the broad-line clouds. The moderate-luminosity AGN is often outshined by the nuclear starburst (e.g., in the radio and $24\ \mu\text{m}$ infrared, as well as soft $0.5\text{--}1.5$ keV X-ray emission), and both the infrared and X-ray emission result from the complex interplay of the stellar and AGN emission modified by intrinsic absorption, as well as absorption related to orientation of the inner spiral with respect to our line of sight.

ACKNOWLEDGEMENTS

This project has been partly funded by the DFG Priority Programme 1177 "Galaxy Evolution". We thank Peter Predehl for useful discussions and a critical reading of the manuscript.

This work is based on observations obtained with *XMM-Newton*, an ESA science mission with instruments and contributions directly funded by ESA Member States and the US (NASA). In Germany, the *XMM-Newton* project is supported by the Bundesministerium für Wirtschaft und Technologie/Deutsches Zentrum für Luft- und Raumfahrt (BMWi/DLR, FKZ 50 OX 0001) and the Max-Planck Society. It is also based on an observation obtained with the *Chandra* X-ray telescope (a NASA mission).

REFERENCES

- Alloin, D., Edmunds, M. G., Lindblad, P. O., & Pagel, B. E. J. 1981, *A&A*, 101, 377
 Brandl, B. R., et al. 2006, *ApJ*, 653, 1129
 Buote, D. A., & Fabian, A. C. 1998, *MNRAS*, 296, 977
 Cappellaro, E., & Turatto, M. 2001, *The Influence of Binaries on Stellar Population Studies*, 264, 199
 Chen, P. S., Fu, H. W., & Gao, Y. F. 2005, *New Astronomy*, 11, 27
 Condon, J. J., Cotton, W. D., Greisen, E. W., Yin, Q. F., Perley, R. A., Taylor, G. B., & Broderick, J. J. 1998, *AJ*, 115, 1693
 Donato, D., et al. 2001, *ApJ*, 375, 739
 Edmunds, M. G., & Pagel, B. E. J. 1982, *MNRAS*, 198, 1089
 Edmunds, M. G., Taylor, K., & Turtle, A. J. 1988, *MNRAS*, 234, 155
 Fabbiano, G. 2002, *Chemical Enrichment of Intracluster and Intergalactic Medium*, 253, 93
 Fiore, F., et al. 2001, *MNRAS*, 327, 771
 Forbes, D. A., & Norris, R. P. 1998, *MNRAS*, 300, 757
 Galliano, E., Alloin, D., Pantin, E., Lagage, P. O., & Marco, O. 2005, *A&A*, 438, 803
 Galliano, E., Alloin, D., Pantin, E., Granato, G. L., Delva, P., Silva, L., Lagage, P. O., & Panuzzo, P. 2008, *A&A*, 492, 3
 Heckman, T. M., Dahlem, M., Eales, S. A., Fabbiano, G., & Weaver, K. 1996, *ApJ*, 457, 616
 Hjelm, M., & Lindblad, P. O. 1996, *A&A*, 305, 727
 Iyamoto, N., Makishima, K., Fukazawa, Y., Tashiro, M., & Ishisaki, Y. 1997, *PASJ*, 49, 425
 Kennicutt, R. C., Jr. 1998, *ApJ*, 498, 541
 Komossa, S., & Schulz, H. 1998, *A&A*, 339, 345
 Kristen, H., Jorsater, S., Lindblad, P. O., & Boksenberg, A. 1997, *A&A*, 328, 483
 Lamer, G., Brunner, H., & Staubert, R. 1996, *A&A*, 311, 384
 Lindblad, P. O. 1999, *A&Ar*, 9, 221
 Lonsdale, C. J., & Helou, G. 1985, *Cataloged Galaxies and Quasars Observed in the IRAS Survey*, Jet Propulsion Laboratory, Pasadena
 Lutz, D., Maiolino, R., Spoon, H. W. W., & Moorwood, A. F. M. 2004, *A&A*, 418, 465
 Mannucci, F., et al. 2003, *A&A*, 401, 519
 Massaro, E., Perri, M., Giommi, P., Nesci, R., & Verrecchia, F. 2004, *A&A*, 422, 103
 Massaro, E., et al. 2003, *A&A*, 399, 33
 Mauch, T., Murphy, T., Buttery, H. J., Curran, J., Hunstead, R. W., Piestrzynski, B., Robertson, J. G., & Sadler, E. M. 2003, *MNRAS*, 342, 1117
 Moorwood, A., et al. 1998, *The Messenger*, 94, 7
 Ogle, P. M., Marshall, H. L., Lee, J. C., & Canizares, C. R. 2000, *ApJL*, 545, L81
 Ogle, P. M., Brookings, T., Canizares, C. R., Lee, J. C., & Marshall, H. L. 2003, *A&A*, 402, 849
 Ott, J., Weiß, A., Henkel, C., & Walter, F. 2005, *AIP Conf. Proc. 783: The Evolution of Starbursts*, 783, 141
 Perlman, E., et al. 2005, *ApJ*, 625, 727
 Perri, M., et al. 2003, *A&A*, 407, 453
 Piccinotti, G., Mushotzky, R. F., Boldt, E. A., Holt, S. S., Marshall, F. E., Serlemitsos, P. J., & Shafer, R. A. 1982, *ApJ*, 253, 485
 Ranalli, P., Comastri, A., & Setti, G. 2003, *A&A*, 399, 39
 Read, A. M. 2006, *Populations of High Energy Sources in Galaxies*, 230, 129
 Rector, T. A., Stocke, J. T., Perlman, E. S., Morris, S. L., & Gioia, I. M. 2000, *AJ*, 120, 1626
 Risaliti, G., Elvis, M., Fabbiano, G., Baldi, A., & Zezas, A. 2005, *ApJL*, 623, L93
 Risaliti, G., Bianchi, S., Matt, G., Baldi, A., Elvis, M., Fabbiano, G., & Zezas, A. 2005, *ApJL*, 630, L129

Risaliti, G., Elvis, M., Fabbiano, G., Baldi, A., Zezas, A., & Salvati, M. 2007, *ApJ*, 659, L111

Risaliti, G., et al. 2008, *MNRAS*, L143

Sakamoto, K., Ho, P. T. P., Mao, R.-Q., Matsushita, S., & Peck, A. B. 2007, *ApJ*, 654, 782

Sandqvist, A., Joersaeter, S., & Lindblad, P. O. 1995, *A&A*, 295, 585

Sandqvist, A., Elfhag, T., & Jorsater, S. 1988, *A&A*, 201, 223

Schurch, N. J., Warwick, R. S., Griffiths, R. E., & Kahn, S. M. 2004, *MNRAS*, 350, 1

Schulz, H., Knake, A., & Schmidt-Kaler, T. 1994, *A&A*, 288, 425

Schulz, H., Komossa, S., Schmitz, C., Mucke, A. 1999, *A&A*, 346, 764

Silich, S., Tenorio-Tagle, G., & Añorve-Zeferino, G. A. 2005, *ApJ*, 635, 1116

Soria, R., Baldi, A., Risaliti, G., Fabbiano, G., King, A., La Parola, V., & Zezas, A. 2007, *MNRAS*, 379, 1313

Stevens, I. R., Forbes, D. A., & Norris, R. P. 1999, *MNRAS*, 306, 479

Stocke, J. T., et al. 1991, *ApJs*, 76, 813

Storchi-Bergmann, T., & Bonatto, C. J. 1991, *MNRAS*, 250, 138

Strateva, I. V., Komossa, S. 2009, *ApJ*, 692, 443, 2009

Strickland, D. K., Heckman, T. M., Colbert, E. J. M., Hoopes, C. G., & Weaver, K. A. 2004, *ApJ*, 606, 829

Spergel, D. N., et al. 2003, *ApJs*, 148, 175

Turner, T. J., Urry, C. M., & Mushotzky, R. F. 1993, *ApJ*, 418, 653

Urry, C. M., et al. 2000, *ApJ*, 532, 816

van Buren, D., & Greenhouse, M. A. 1994, *ApJ*, 431, 640

Veron, P., Lindblad, P. O., Zuiderwijk, E. J., Veron, M. P., & Adam, G. 1980, *A&A*, 87, 245

Veilleux, S., Shopbell, P. L., Rupke, D. S., Bland-Hawthorn, J., & Cecil, G. 2003, *AJ*, 126, 2185

Voges, W., et al. 1999, *A&A*, 349, 389

Wang, Q. D., Immler, S., Walterbos, R., Lauroesch, J. T., & Breitschwerdt, D. 2001, *ApJ*, 555, L99

Wang, Q. D. 2003, *High Energy Processes and Phenomena in Astrophysics*, 214, 32

Wang, J., Fabbiano, G., Elvis, M., Risaliti, G., Mazzarella, J. M., Howell, J. H., & Lord, S. 2009, arXiv:0901.0297

Ward, M. J., Done, C., Fabian, A. C., Tennant, A. F., & Shafer, R. A. 1988, *ApJ*, 324, 767

APPENDIX A: MS 0331.3–3629

A1 *Chandra* and *XMM-Newton* Imaging Spectroscopy of MS 0331.3–3629

We present a series of high-quality (up to $\sim 2 \times 10^4$ counts) X-ray imaging spectra of the high-peaked BL Lac (HBL) MS 0331.3–3629. MS 0331.3–3629 (03:33:12.2, –36:19:48.0) is a $z = 0.308$ blazar candidate (Stocke et al. 1991) which was serendipitously detected in six recent long exposures of NGC 1365 – falling within one *Chandra* and five *XMM-Newton* fields. Table A1 shows a summary of the recent *Chandra* and *XMM-Newton* observations of MS 0331.3–3629. We used standard *Chandra* and *XMM-Newton* pipeline reductions to obtain X-ray spectra

Table A1. MS 0331.3–3629: *Chandra/XMM-Newton* Observation Summary. (1) Observation ID; (2) Modified Julian Day; (3) Total counts; (4) Effective exposure time, after corrections for flaring and chip position.

ObsID (1)	MJD (2)	Counts (3) 0.3–10 keV	T_{eff} (4) 10^3 s
		ACIS-I2	ACIS-I2
		pn MOS1 MOS2	pn MOS1 MOS2
3554	52632	2758	14.6
0151370101	52655	5888 2767 2700	12.7 17.4 17.4
0151370201	52679	... 712 675	... 5.1 5.0
0151370701	52864	... 843 754	... 8.1 8.2
0205590301	53021	18088 6006 6631	48.7 57.3 57.4
0205590401	53210	8700 4182 3713	28.6 46.4 47.1

(grouped into bins of at least 20 counts per bin) of the blazar from an elliptical region with a semi-major axis of $90''$ for the pn and $60''$ for the MOS cameras (for an off axis angle $\sim 12.5'$). About half of the exposure time of ObsID 0205590401 is lost to flares, while for ObsID 0151370201 and ObsID 0151370701 the BL Lac falls within the chip-gaps of the pn camera, and we use the MOS data only.

The 0.3–10 keV spectra can be fit by single power-law models modified by Galactic absorption. The fit parameters are given in the top portion of Table A1. The fits to the two highest quality *XMM-Newton* spectra can be improved by adding an intrinsic absorber $N_{\text{H},i} \approx 2 \times 10^{20} \text{ cm}^{-2}$ (F-test probability of 1×10^{-7} and 2×10^{-3} for ObsID 0205590301 and ObsID 0205590401, respectively; last two rows of Table A1). The best spectral fits of all spectra (including intrinsic absorption in the case of the two longest *XMM-Newton* exposures) are shown in Figure A1. Broken power-law fits (*bknpow* in XSPEC) are also consistent with the *XMM-Newton* observations (an F-test shows no improvement to the model fit for the *Chandra* observation) and the fit results are presented in Table A3. For the five *XMM-Newton* fits, the break energy is around $\langle E_{\text{break}} \rangle \approx 1.1 \text{ keV}^7$, the soft photon index $\langle \Gamma_1 \rangle \approx 1.9$, and hard photon index $\langle \Gamma_2 \rangle \approx 2.1$, although all values show large variations between the different observations. The current data cannot distinguish between the intrinsic absorption and broken power-law fit scenarios; the broken power-law fits have one extra parameter but do not provide statistically better fits in comparison to the intrinsically-absorbed fits, except for ObsID 0205590401 (an F-test probability of 2×10^{-3}).

A2 X-ray Spectral Curvature of MS 0331.3–3629

Perlman et al. (2005) suggest that a large fraction of BL Lacs show spectral curvature in the 0.5–10.0 keV band, which can be detected using spectral fits in consecutive energy bands. This spectral curvature requires a change in the standard energy emission mechanism (which produces a simple power-law), and Perlman et al. (2005) propose to explain this curvature by an episodic (or time-variable)

⁷ $\langle \rangle$ indicate weighted averages.

Table A2. MS 0331.3–3629: 0.3–10 keV Band Single Power-law Spectroscopic Fits. (1) Observation ID; (2) Hard-band rest-frame absorption-corrected ACIS-S or MOS/pn average fluxes in units of 10^{-13} erg s $^{-1}$ cm $^{-2}$; (3) Soft-band rest-frame absorption-corrected ACIS-S or MOS/pn average fluxes in units of 10^{-13} erg s $^{-1}$ cm $^{-2}$; (4) Power-law photon index; (5) Intrinsic absorption in units of 10^{20} cm s $^{-1}$ (6) Model fit: “PL” indicates a power law fit [wabs*zpov in XSPEC], “APL” indicates a power law fit including intrinsic absorption [wabs*(zwabs*zpov) in XSPEC]. A cold absorber equal to the Galactic value, $N_{\text{H}} = 1.4 \times 10^{20}$ cm $^{-2}$, is included in the fits in all cases; (7) Data used in the model fits; (8) χ^2 per degree of freedom (DoF).

ObsID (1)	$F_{2-10 \text{ keV}}$ (2)	$F_{0.5-2 \text{ keV}}$ (3)	Γ (4)	$N_{\text{H},i}$ (5)	Model (6)	Data (7)	χ^2/DoF (8)
3554	$19.6^{+0.1}_{-0.1}$	$20.5^{+0.2}_{-0.2}$	2.06 ± 0.04	...	PL	ACIS-S	123/111
0151370101	$20.8^{+0.7}_{-0.5}$	$16.8^{+0.4}_{-0.5}$	1.95 ± 0.02	...	PL	pn+MOS	490/462
0151370201	$15.3^{+1.4}_{-1.6}$	$17.8^{+1.4}_{-1.2}$	2.00 ± 0.05	...	PL	MOS	60/63
0151370701	$16.4^{+1.4}_{-1.3}$	$17.0^{+1.4}_{-1.1}$	2.08 ± 0.04	...	PL	MOS	78/77
0205590301	$14.9^{+0.5}_{-0.6}$	$18.1^{+0.5}_{-0.5}$	1.97 ± 0.01	...	PL	pn+MOS	967/953
0205590401	$16.2^{+0.5}_{-0.6}$	$16.6^{+0.5}_{-0.5}$	2.08 ± 0.01	...	PL	pn+MOS	622/664
0205590301	$16.2^{+0.4}_{-0.4}$	$17.6^{+1.0}_{-0.2}$	2.05 ± 0.02	2.4 ± 0.5	APL	pn+MOS	939/952
0205590401	$17.4^{+0.4}_{-0.4}$	$16.0^{+1.0}_{-0.2}$	2.16 ± 0.02	2.0 ± 0.1	APL	pn+MOS	612/663

particle acceleration process. Using the highest signal-to-noise best *XMM-Newton* spectrum of MS 0331.3–3629 (Obs ID 0205590301), we looked for signs of curvature similar to those found by Perlman et al. (2005). MS 0331.3–3629 shows no clear signs of spectral curvature in the 0.5–10 keV range. In addition, with the exception of Obs ID 0205590401, the broken power-law fit results, which are not preferable to a simple absorbed power law, suggest that varying the photon index with energy bandpass is not necessary to describe the X-ray spectra. Following Perlman et al. (2005), this could mean that the radio to soft-X-ray emission of MS 0331.3–3629 is consistent with synchrotron radiation produced by electrons with a simple power-law distribution.

A3 Previous X-ray observations of MS 0331.3–3629

MS 0331.3–3629 was serendipitously detected in eight *ROSAT* observations (see Table A4). We performed source detection and photometry on the 4 PSPC (channels 52–201, corresponding to 0.5–2.0 keV) and 3 HRI (channels 0–15, 0.1–2.4 keV) event files using EXSAS. The resulting count rates and 0.5–2.0 keV fluxes (assuming $\Gamma = 2$) are given in Table A4. The RASS detection quoted in Table A4 was obtained from the *ROSAT* bright source catalog (Voges et al. 1999). Lamer et al. (1996) used the longest PSPC exposure to measure a photon index in the 0.1–2.4 keV band, $\Gamma_{\text{soft}} = 2.1 \pm 0.15$. Table A5 gives the soft-band (0.1–2.5 keV in the case of *ROSAT* PSPC) spectral fits obtained with XSPEC in a manner identical to the one used for the *Chandra/XMM-Newton* X-ray spectra. We used standard EXSAS processing to obtain the spectra, varying the size of the extraction region to include 90% of the flux in each case. A simple power-law fit (indicated with “PL” in Table A5) with absorption equal to the Galactic value and a photon index between 1.8 and 2.1 is sufficient to represent the soft-band *ROSAT* PSPC spectra in three of the four cases. In the case of RP700921A01, the PL fit is only marginally acceptable ($\chi^2/\text{DoF} = 53/40$, null hypothesis probability of 8%). The

inclusion of intrinsic absorption does not improve the model fits.

MS 0331.3–3629 was also observed by *BeppoSAX* (S/N=3.3) and is part of the HELLAS sample (Fiore et al. 2001). Rector et al. (2000) show the optical spectrum of MS 0331.3–3629 as part of the *Enstein* medium sensitivity survey BL Lac catalog. The *Enstein* flux was $F_{0.3-3.5 \text{ keV}} = 5.22 \times 10^{-13}$ erg s $^{-1}$ cm $^{-2}$, consistent with the values listed in Table A5.

A4 X-ray variability of MS 0331.3–3629

The MS 0331.3–3629 X-ray flux is variable on timescales of weeks to years. The soft (0.5–2.0 keV) band variability is about a factor of 2 over 7.5 years (rest-frame); the hard (2–10 keV) band variations appear smaller, but the time interval probed is also shorter. Only the *Chandra* observation shows short term count-rate variability of about 20% on timescale of hours, but the evidence for this short term variability is not consistent: the Kolmogorov-Smirnov test confirms it with a 97% confidence, but a χ^2 test gives a $\sim 60\%$ probability of constancy. The power-law photon index also varies between the observations on timescales of days to years.

A5 Multiwavelength Observations and the Nature of MS 0331.3–3629

The optical spectrum of MS 0331.3–3629 shows no emission lines and has a Ca II H&K break of 30% (Stocke et al. 1991), consistent with a BL Lac classification at $z = 0.308$. An HST observation, taken on 1996 October 29, revealed an elliptical host which outshines the active nucleus at 7020 Å (the host apparent magnitude is $R = 17.83$, compared to $R = 19.03$ for the active nucleus, Urry et al. 2000). Note that most prior work on the optical-to-X-ray and optical-to-radio flux ratios used the total galaxy magnitude in the optical, leading to incorrect estimates. The radio-to-X-ray index, defined as $\alpha_{\text{rx}} = -\log[F_{5\text{GHz}}/F_{1\text{keV}}]/\log[\nu_{5\text{GHz}}/\nu_{1\text{keV}}]$, is $\alpha_{\text{rx}} = 0.55$.

MS 0331.3–3629 has been observed in the J, H, and K bands (2MASS, likely dominated by the host galaxy, Chen et al. 2005), and the radio: the VLA (Stoche et al. 1991), NVSS (observed on 1993-10, Condon et al. 1998), SUMMS (1998/12–2002/08 composite, Mauch et al. 2003). If we construct a spectral energy distribution (SED) based on these heterogeneous and non-concurrent observations, it peaks at $\log(\nu_p) \approx 17.0$, and MS 0331.3–3629 has the appearance of a high energy peaked blazar (Donato et al. 2001). Assuming that the radio to soft X-ray emission is dominated by synchrotron emission, a log-parabolic fit to the SED is possible (see for e.g., Massaro et al. 2003, 2004). Under the log-parabolic model, the bolometric luminosity of the synchrotron component can be estimated analytically (e.g., Perri et al. 2003; Massaro et al. 2004), $L_{\text{Synch}} \approx 4 \times 10^{45} \text{ erg s}^{-1}$.

Table A3. MS 0331.3–3629: 0.3–10 keV Band Broken Power-law Spectral Fits. (1) Observation ID; (2) Hard-band rest-frame absorption-corrected ACIS-S or MOS/pn average fluxes in units of 10^{-13} erg s $^{-1}$ cm $^{-2}$; (3) Soft-band rest-frame absorption-corrected ACIS-S or MOS/pn average fluxes in units of 10^{-13} erg s $^{-1}$ cm $^{-2}$; (4) First and (5) Second power-law photon indices; (6) Break energy, in keV; (7) χ^2 per degree of freedom (DoF).

ObsID (1)	$F_{2-10\text{ keV}}$ (2)	$F_{0.5-2\text{ keV}}$ (3)	Γ_1 (4)	Γ_2 (5)	E_{break} (6)	χ^2/DoF (7)
3554	$20.6^{+0.2}_{-0.1}$	$15.4^{+1.8}_{-1.0}$	2.16 ± 0.08	1.95 ± 0.11	1.7 ± 0.7	120/109
0151370101	$19.3^{+0.4}_{-0.3}$	$16.0^{+0.7}_{-1.0}$	1.91 ± 0.04	2.01 ± 0.04	1.3 ± 0.5	486/460
0151370201	$16.5^{+3.2}_{-3.7}$	$15.4^{+1.8}_{-1.0}$	1.87 ± 0.12	2.2 ± 0.2	1.4 ± 0.6	57/61
0151370701	$16.9^{+6.3}_{-2.9}$	$15.5^{+1.9}_{-2.4}$	2.03 ± 0.06	2.3 ± 0.3	2.4 ± 1.5	76/75
0205590301	$15.2^{+0.9}_{-0.9}$	$17.1^{+0.7}_{-0.7}$	1.87 ± 0.03	2.05 ± 0.02	1.1 ± 0.1	937/951
0205590401	$16.6^{+0.9}_{-0.9}$	$15.2^{+0.7}_{-0.7}$	1.99 ± 0.03	2.20 ± 0.04	1.2 ± 0.2	605/662

Table A4. MS 0331.3–3629: *ROSAT* Photometry. (1) *ROSAT* observation ID, where “RP” refers to the PSPC, “RH” to the HRI, and “RS” to the *ROSAT* all sky survey; (2) Observation date; (3) Effective exposure time; (4) Off-axis angle; (5) Count rate in the observed 0.5–2.0 keV band (PSPC) or 0.1–2.4 keV band (HRI); (6) Rest-frame 0.5–2.0 keV absorption-corrected flux.

ObsID (1)	Date (2) yy-mm-dd	T_{eff} (3) s	OffAngle (4) '	CR (5) counts s $^{-1}$	$F_{0.5-2\text{ keV}}$ (6) 10^{-13} erg s $^{-1}$ cm $^{-2}$
RP800301N00	1992-08-22	840	43.1	0.087 ± 0.011	10 ± 1.3
RP700921N00	1992-08-23	2323	12.4	0.090 ± 0.006	11 ± 0.7
RP800301A01	1993-02-02	4121	43.1	0.048 ± 0.004	5.7 ± 0.5
RP700921A01	1993-02-10	6908	12.4	0.062 ± 0.003	7.5 ± 0.4
RH701297N00	1994-08-04	9182	12.4	0.037 ± 0.002	7.9 ± 0.5
RH701297A01	1994-08-23	323	12.4	0.032 ± 0.011	6.8 ± 2.3
RH701297A02	1995-07-04	9074	12.4	0.037 ± 0.002	7.9 ± 0.5
RS932309N00	1990-07-30	172	...	0.090 ± 0.028	5.2 ± 1.7

Table A5. MS 0331.3–3629: Soft-band Spectroscopic Fits. (1) Observation ID; (2) Soft-band power-law photon index; (3) Rest-frame 2 keV monochromatic flux density; (4) Rest-frame absorption-corrected fluxes; (5) Bandpass used in the model fit; (6) Model fit: “PL” indicates a power law fit [wabs*zpov in XSPEC], “APL” indicates a power law fit including intrinsic absorption [wabs*(zwabs*zpov) in XSPEC] with $N_{\text{H},i} = 2.0 \pm 0.5 \times 10^{20}$ cm $^{-2}$. A cold absorber equal to the Galactic value, $N_{\text{H}} = 1.4 \times 10^{20}$ cm $^{-2}$ is included in the fits in all cases; (7) χ^2 per degree of freedom (DoF).

ObsID (1)	Γ_{soft} (2)	$f_{2\text{ keV}}$ (3) 10^{-8} Jy	$F_{0.5-2\text{ keV}}$ (4) 10^{-13} erg s $^{-1}$ cm $^{-2}$	Data (5) keV	Model (6)	χ^2/DoF (7)
RP800301N00	1.81 ± 0.28	2.9 ± 0.7	17^{+8}_{-7}	0.1–2.4	PL	6/7
RP700921N00	1.91 ± 0.09	2.9 ± 0.3	18^{+2}_{-3}	0.1–2.4	PL	31/37
RP800301A01	1.91 ± 0.12	1.8 ± 0.3	11^{+3}_{-2}	0.1–2.4	PL	19/20
RP700921A01	2.10 ± 0.05	1.9 ± 0.2	14^{+2}_{-2}	0.1–2.4	PL	53/40
3554	2.12 ± 0.06	2.7 ± 0.2	$19.9^{+1.9}_{-2.0}$	0.2–2.5	PL	97/87
0151370101	1.92 ± 0.02	2.7 ± 0.1	$15.9^{+1.2}_{-1.1}$	0.2–2.5	PL	427/411
0151370201	1.87 ± 0.06	2.5 ± 0.2	$15.1^{+2.3}_{-2.3}$	0.2–2.5	PL	59/55
0151370701	2.05 ± 0.06	2.4 ± 0.2	$16.6^{+2.1}_{-1.9}$	0.2–2.5	PL	72/71
0205590301	2.04 ± 0.03	2.3 ± 0.1	$16.0^{+1.0}_{-1.1}$	0.2–2.5	APL	802/784
0205590301	1.93 ± 0.01	2.3 ± 0.1	$14.8^{+0.6}_{-0.6}$	0.2–2.5	PL	821/785
0205590401	2.06 ± 0.02	2.3 ± 0.1	$16.3^{+0.8}_{-0.9}$	0.2–2.5	PL	517/573

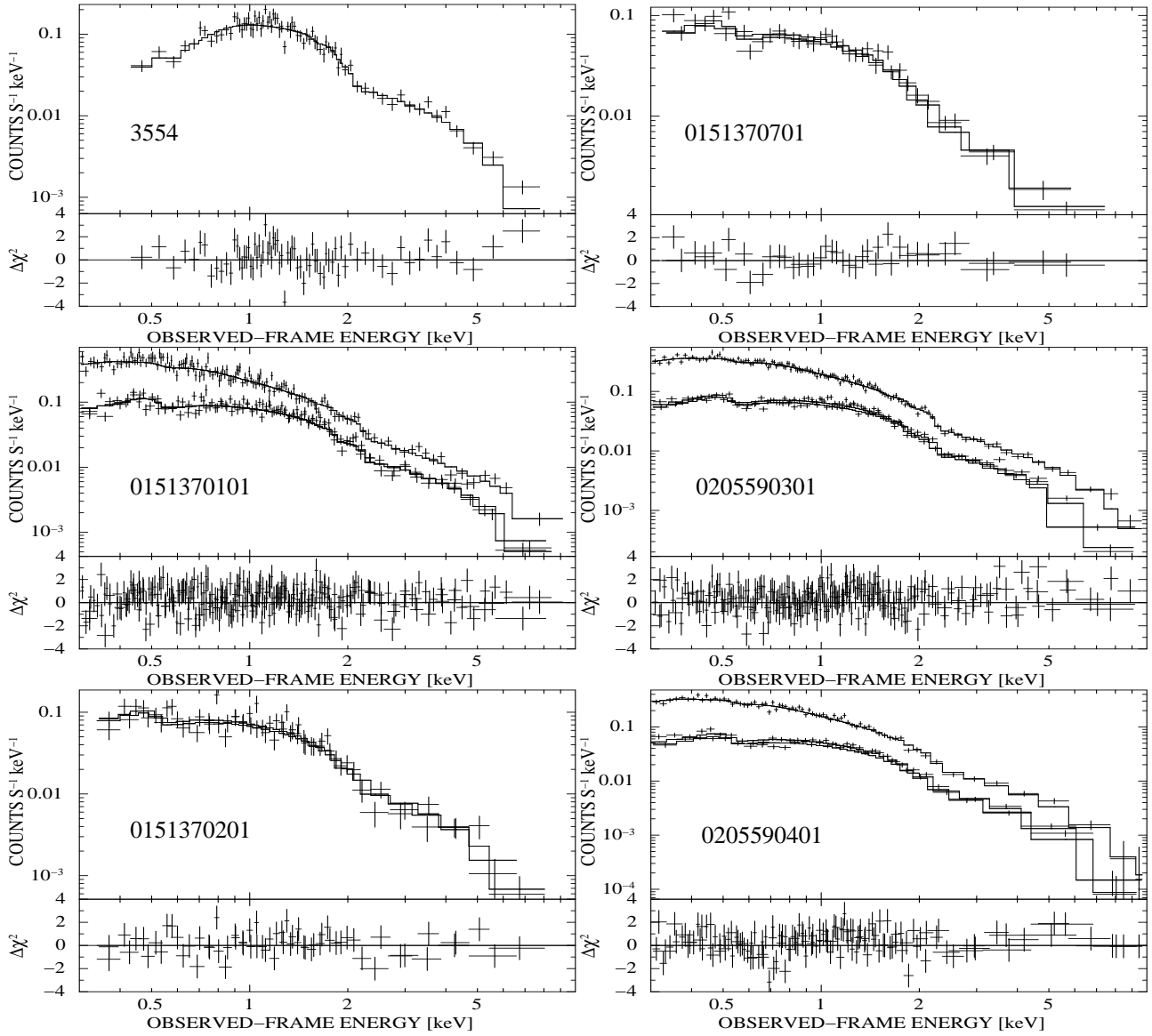


Figure A1. The 0.3–10 keV spectral fits of MS 0331.3–3629. In each case, the top panel shows the spectrum and best fit model from Table A1 as well as the ObsID, the bottom panel – the fit residuals.